MNRAS **000**, 1–9 (2016) Preprint 16 September 2016 Compiled using MNRAS LATEX style file v3.0

Extending Semi-numeric Reionisation Models to the First Stars and Galaxies

Daegene Koh,[1]⋆ John H. Wise,[1]†
[1] *Center for Relativistic Astrophysics, Georgia Institute of Technology, 837 State Street, Atlanta, GA 30332, USA*

arXiv:1609.04400v1 [astro-ph.CO] 14 Sep 2016

16 September 2016

ABSTRACT

Semi-numeric methods have made it possible to efficiently model the epoch of reionisation (EoR). While most implementations involve a reduction to a simple three-parameter model, we introduce a new mass-dependent ionising efficiency parameter that folds in physical parameters that are constrained by the latest numerical simulations. This new parameterization enables the effective modeling of a broad range of host halo masses containing ionising sources, extending from the smallest Population III host halos with $M \sim 10^6 M_\odot$, which are often ignored, to the rarest cosmic peaks with $M \sim 10^{12} M_\odot$ during EoR. We compare the resulting ionising histories with a typical three-parameter model and also compare with the latest constraints from the *Planck* mission. Our model results in a optical depth due to Thomson scattering, τ_e = 0.057, that is consistent with *Planck*. The largest difference in our model is shown in the resulting bubble size distributions which peak at lower characteristic sizes and are broadened. We also consider the uncertainties of the various physical parameters and comparing the resulting ionising histories broadly disfavors a small contribution from galaxies. As the smallest haloes cease a meaningful contribution to the ionising photon budget after z = 10, implying they play a role in determining the start of EoR and little else, an ionising photon escape fraction greater than 0.6 is also broadly disfavored.

Key words: dark ages, reionization, first stars – galaxies:high-redshift – early Universe – stars: Population III – cosmology:theory

1 INTRODUCTION

Models of the Epoch of Reionisation (EoR) have been extensively improved over the years as tighter observational constraints are provided. This particular phase transition of the universe can provide a number of insights into the details of the beginnings of structure formation (e.g. Robertson et al. 2010).

The biggest current observational constraints in modeling EoR comes from the Thomson scattering optical depth, τ_e, to the cosmic microwave background (CMB). Improvements to the measurement have progressively driven down this particular value, where the latest results estimate τ_e = 0.0596 ± 0.0089 corresponding to a redshift of instantaneous reionsation of $z = 8.0^{+0.9}_{-1.1}$ (Planck Collaboration et al. 2016a). Next, the transmission fraction of quasar light through the intergalactic medium shows that the EoR ended by z ∼ 6 (Gunn & Peterson 1965; Fan et al. 2006), though there are some recent observations implying that it may not have been completed until z ∼ 5.6 (Mesinger 2010; Becker et al. 2015). Interestingly, it was previously expected that quasars alone could not produce the needed number of ionising photons to complete reionisation as earlier constraints from Wilkinson Microwave Anisotropy Probe (WMAP) introduced a need for high-redshift sources (e.g. Willott et al. 2010; Grissom et al. 2013). However, with the updated Planck results requiring a later start to reionisation, quasars have come back in recent models, in some of which they are the only sources (Madau & Haardt 2015).

Theoretical efforts in the modeling EoR has ranged from relative simple analytic models (Madau et al. 1999; Kuhlen & Faucher-Giguere 2012; Alvarez et al. 2012) all the way to high-resolution numerical simulations with various detailed star and galaxy formation prescriptions that include self-consistent ray tracing (Iliev et al. 2007; Trac & Gnedin 2011). Reionisation necessitates a large number of approaches due to the wide range of scales involved in the

⋆ E-mail: dkoh30@gatech.edu
† E-mail: jwise@gatech.edu

© 2016 The Authors

process. Moreover, a full numerical solution would require parsec scale resolution to correctly follow sources and feedback in, at minimum, a 100 comoving Mpc^3 box to get convergent histories (Iliev et al. 2014). Such simulations would be an enormous computational cost.

Semi-numeric models are thus an attractive alternative. Such models can accurately generate full three-dimensional density, velocity, and ionisation fields without the need to follow the underlying physics (Furlanetto et al. 2004; Mesinger & Furlanetto 2007; Zahn et al. 2007). These models make the following fundamental assumption that overdense regions drive the ionisation process. With this assumption, one asserts that if the number of available photons exceeds the number of baryons in a cell, the cell must be ionised. This simple model provides a powerful tool that compares favorably with high-resolution radiative transfer numerical simulations (Zahn et al. 2011).

Within the numerous models, there have been many efforts to understand the role of the various potential sources in the reionisation process. Typical models only consider galaxies hosted by atomic-cooling halos above $T_{\rm vir} \sim 10^4$ K. However, an often neglected source is mini-halos with $M < 10^8\ \mathrm{M}_\odot$ containing massive, metal-free Pop III stars. Pop III stars have been studied extensively over the past decade detailing their formation (Abel et al. 2002; Turk et al. 2009; Greif et al. 2011), their spectral properties (Tumlinson & Shull 2000; Schaerer 2002), and their final fates (Woosley & Weaver 1995; Heger & Woosley 2002, 2010). Of more interest to the EoR, these massive stars also produce extended H II regions in their immediate vicinity spanning 1-3 kpc (Kitayama et al. 2004; Whalen et al. 2004; Alvarez et al. 2006; Abel et al. 2007). These H II regions will then grow out further as mini-halos merge together to form the first galaxies providing additional ionising flux. Ahn et al. (2012) used a sub-grid model to populate mini-halos in a 114 Mpc h^{-1} simulation and showed their addition had a significant effect in determining the onset of reionisation. Furthermore, Wise et al. (2014) calculated the escape fraction of ionising photons in a 1 comoving Mpc radiation hydrodynamics simulation showing that mini-halos can contribute up to 30 percent of the ionising photon budget.

Given the extensive volume of data available from large volume high-resolution simulations at high redshifts, we can take simulated physical properties of ionising sources, such as the photon escape fraction and star formation efficiency. In this work, we take these calculated properties to create a new parameterization extending existing semi-numeric models to include the effects of mini-halos.

In the immediately following Section 2, we introduce our new parameterization. In Section 3, we compare the ionisation histories produced from our model and show the resulting bubble size distributions. Finally, in section 4, we provide a short discussion and summarize our results.

2 METHODS

2.1 Simulating Reionisation

Our treatment involves use of the semi-numerical reionisation simulation code 21CMFAST (Mesinger et al. 2011). In this code, the ionisation field is generated following an excursion-set approach (Furlanetto et al. 2004). Namely, a cell is considered to be ionised when

$$f_{\rm coll}(x, M_{\rm min}, R, z) \geq \zeta^{-1} \tag{1}$$

where ζ is the ionisation efficiency, and $f_{\rm coll}$ is the fraction of collapsed mass inside a region of size R in halos whose mass is greater than $M_{\rm min}$ (Mesinger & Furlanetto 2007; Zahn et al. 2007). This value R is iterated from $R_{\rm max}$, which is typically taken to be the maximum horizon of ioinising photons, or the effective mean free path down to the length of a single cell. These three parameters then fully determine the ionisation state at any given redshift. Our simulations are run on a box with a 100 comoving Mpc side length using 2048^3 cells downsampled to 1024^3 cells to generate the ionisation field. The main contribution in this work is our detailed treatment of the parameter ζ which is outlined in the following sections.

2.2 Calculating the Ionising Efficiency

In previous treatments, ζ typically represents a homogeneous ionising efficiency factor for all star-forming galaxies in any environment. A typical parameterization is provided in Greig & Mesinger (2016) as

$$\zeta = 30 \left(\frac{f_{\rm esc}}{0.2}\right)\left(\frac{f_*}{0.03}\right)\left(\frac{f_{\rm b}}{\Omega_{\rm b}/\Omega_{\rm m}}\right)\left(\frac{N_{\gamma/{\rm b}}}{4000}\right)\left(\frac{1.5}{1+n_{rec}}\right) \tag{2}$$

where $f_{\rm esc}$ is the fraction of ionising photons escaping into the intergalactic medium (IGM), f_* is the fraction galactic gas in stars, $f_{\rm b}$ is the baryon fraction inside haloes hosting galaxies in units of the cosmic baryon fraction, $N_{\gamma/{\rm b}}$ is the number of ionising photons per baryon in stars, and $n_{\rm rec}$ is the average number of recombinations per baryon in the IGM. These values are all assumed to be mass- and redshift-independent to produce a single ζ value. We take this model to be the Fiducial case and compare our new parameterization against it in Sec 3.

The main improvement of this work is to model ζ as a function of the host halo mass at a given redshift. This class of parameterizations has been initially explored by Furlanetto et al. (2005) but they only considered a simple power-law function setting $\zeta \sim m^\alpha$ for various values of α. In our work, we consider a more extensive dependence on the host halo mass that is better physically motivated. This allows us to incorporate the distribution of ionising efficiencies at different masses as well including the contribution of mini-halos to the photon budget for reionisation.

In particular, ζ has been parameterized as follows.

$$\zeta(M_{vir}) = \begin{cases} \zeta_{0,3}\ f_{\rm esc}\ f_*\ N_{3,\gamma/{\rm b}}\ f_{t*} & M_{\rm min} \leq M_{\rm vir} < M_{\rm filter} \\ \zeta_{0,2}\ f_{\rm esc}(M_{\rm h})\ f_*(M_{\rm h})\ f_{\rm occ}(M_{\rm h})\ N_{2,\gamma/{\rm b}} & M_{\rm vir} \geq M_{\rm filter} \end{cases} \tag{3}$$

where $N_{3,\gamma/{\rm b}}$ is $N_{\gamma/{\rm b}}$ for Pop III stars, f_{t*} is the fractional star-formation timescale for Pop III stars, $f_{\rm occ}$ is the fraction of halos containing star-forming galaxies, and $N_{2,\gamma/{\rm b}}$ is $N_{\gamma/{\rm b}}$ for galaxies. Lastly, $\zeta_{0,3}$ and $\zeta_{0,2}$ are constants calibrated to the desired reionisation history. In this work, we take these values to be 2 and 3 respectively.

Furthermore, the domain of ζ is characterized by two

different masses. First is $M_{\rm min}$, which is the minimum mass of mini-halos that is required to collapse to form Pop III stars. This mass is determined by the strength of the soft H_2 photodissociating Lyman-Werner (LW) flux by

$$M_{\rm min}(\mathrm{F_{LW}}) = 1.25 \text{ x } 10^5 + 8.7 \text{ x } 10^5 \left(\frac{\mathrm{F_{LW}}}{10^{-21}}\right)^{0.47} \quad (4)$$

taken from Machacek et al. (2001), where $\mathrm{F_{LW}}$ is the strength of the LW background in units of erg $\mathrm{s^{-1}}$ $\mathrm{cm^{-2}}$ $\mathrm{Hz^{-1}}$. The magnitude of this flux as a function of redshift is modeled as

$$\log J_{21}(z) = A + Bz + Cz^2 + Dz^3 + Ez^4 \quad (5)$$

where (A,B,C,D,E) = (-2.567, 0.4562, -0.02680, 5.882 x 10^{-4}, -5.056 x 10^{-6}) taken from Wise et al. (2012a). Here J_{21} is the specific intensity in units of erg $\mathrm{s^{-1}}$ $\mathrm{cm^{-2}}$ $\mathrm{Hz^{-1}}$ $\mathrm{sr^{-1}}$. In this fit, the strength of the background peaks at z = 13.765 with a value of J_{21} = 0.97 after which galaxies would dominate the contribution. As the actual minimum mass for collapse would be dependent on the exact environment of the halos, we set the LW background to be this maximum value of this fit at subsequent redshifts. At these redshifts, the exact value has minimal impact on the resulting reionisation history because galaxies provide the bulk of the photon budget.

The other relevant characteristic mass is the filtering mass, $M_{\rm filter}$, which is the characteristic mass scale below which reionisation suppresses gas fraction in low-mass halos (Gnedin 2000) given by

$$M_{filter}^{2/3} = \frac{3}{a}\int_0^a da' M_J^{2/3}(a')\left[1 - \left(\frac{a'}{a}\right)^{1/2}\right] \quad (6)$$

where M_J is the Jeans mass and a is the cosmological scale factor. We calculated $M_{\rm filter}$ from the simulations of Wise et al. (2012a) and created a polynomial fit as a function of redshift for computational ease given by

$$\log M_{\rm filter}(z) = A + Bz + Cz^2 + Dz^3 \quad (7)$$

where (A,B,C,D) = (9.065, -0.15611, 0.0063, -1.9577 x 10^{-4}). This $M_{\rm filter}$ is then used to as the mass cut-off above which galaxy formation occurs at a given redshift. From $M_{\rm min}$ to $M_{\rm filter}$, we assume Pop III stars are the dominant contributors, while for $M_{\rm vir} > M_{\rm filter}$, galaxies dominate. For the rest of this work, we define mini-halos as halos with masses in the range $M_{\rm min} \leq M_{\rm vir} < M_{\rm filter}$ whose dominant ionising source is Pop III stars.

These characteristic masses are shown in Fig 1. When $M_{\rm filter} > M_{\rm min}$, which happens at z > 24, we set ζ to be 0 as no galaxies can be formed. We can see that our adopted $M_{\rm filter}$ is much less than any of the typically adopted minimum mass values at z > 15, greatly increasing the number of available galaxies to produce ionising photons.

2.2.1 *Mini-halos*

For mini-halos ($M_{\rm min} \leq M_{\rm vir} < M_{\rm filter}$), the photon contribution is assumed to be entirely from Pop III stars. Given the large uncertainty and lack of observational constraints for the relevant parameters for the first stars, we take each value in the parameterization to be mass- and redshift-independent in the relevant ranges for Pop III stars. Instead, we consider the possible range of values in Sec. 2.2.4.

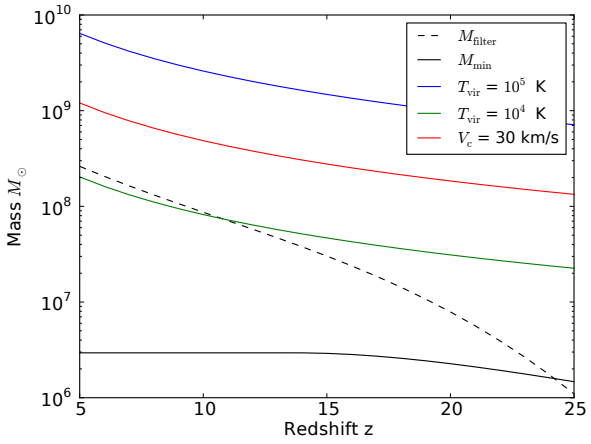

Figure 1. Characteristic masses as a function of redshift. The minimum mass, $M_{\rm min}$ (black, solid), is the mass above which ionising sources exist. The filtering mass, $M_{\rm filter}$ (black, dashed), is the threshold between Pop III mini-halos and galaxies. That is, any mass range between these two lines will be assumed to be a mini-halo, while any mass range above the dashed line will host galaxies. For comparison, we also show commonly assumed minimum masses corresponding to a virial temperature $T_{\rm vir} = 10^4$ K (green), $T_{\rm vir} = 10^5$ K (blue), and circular velocity, V_c = 30 km/s (red).

First, $f_{\rm esc}$ is the parameter with the largest uncertainty (Alvarez et al. 2006), which we adopt a value of 0.6. We set f_* to be a constant at $100\,\mathrm{M_\odot}/10^6\,\mathrm{M_\odot}$ which is a typical ratio found in cosmological simulations of Pop III star formation (Susa et al. 2014; Hirano et al. 2015). The number of photons per baryon, $N_{3,\gamma/\mathrm{b}}$ is largely determined by the surface temperature of the star. We take this value to be 50,000 (Schaerer 2002). Lastly, we introduce a term f_{t*}, the fractional star-formation timescale defined as the average lifetime of a Pop III star over the recovery time, to account for the fact that Pop III formation events are bursty. Pop III stars can very efficiently photoevaporate their surroundings and their supernova completely disrupt the host halo (Greif et al. 2007; Koh & Wise 2016). This results in a significant delay until the subsequent generation of star formation (Jeon et al. 2014). We take this value to be 5 Myr/30 Myr.

2.2.2 *Galaxies*

For halos with $M_{\rm h} > M_{\rm filter}$, galaxies dominate the photon budget following the death of Pop III stars. For this range of masses, we take a number of fits from cosmological galaxy simulations to calculate ζ.

The photon escape fraction, $f_{\rm esc}$, is modeled using the piece-wise fit below

$$\log f_{\rm esc}(M_{vir}) = \begin{cases} -0.51 - 0.039 \log M_{\rm vir} & \log M_{\rm vir} \geq 8.5 \\ 2.669 - 0.413 \log M_{\rm vir} & 7 \leq \log M_{\rm vir} < 8.5 \\ -0.222 & \log M_{\rm vir} < 7 \end{cases}$$

(8)

taken from Kimm & Cen (2014) who used high-resolution zoom-in simulations to construct the fit. This fit takes a nominal value of $f_{\rm esc} = 0.6$ for halos below log $M_{\rm vir}/\,{\rm M}_\odot < 7$, matching our assumed value for mini-halos, with a steep decrease for $7 <$ log $M_{\rm vir}/\,{\rm M}_\odot < 8.5$ and then flattens off for log $M_{\rm vir}/\,{\rm M}_\odot > 8.5$ to $f_{\rm esc} \sim 0.1$. This is consistent with other simulations showing high escape fractions for low mass galaxies (Wise & Cen 2009; Paardekooper et al. 2015).

To determine the stellar mass fraction, we use a combination of fits taken from O'Shea et al. (2015) and Behroozi et al. (2013). From the former, valid for the range log $M_{\rm vir}/\,{\rm M}_\odot < 10$, we have

$$f_*(M_{\rm vir}) = 1.26 \text{ x } 10^{-3} \left(\frac{{\rm M_{vir}}}{10^8\,{\rm M}_\odot} \right)^{0.74} \tag{9}$$

fitted using data from the Renaissance Simulations that focus on galaxy formation during the EoR. These simulations have found that galaxy properties during EoR are largely independent of redshift (Xu et al. 2016a). From the latter, valid for the range log $M_{\rm vir} \geq 10$, we have

$$\log\, f_*(M_{\rm vir}, z = 6) = \log\,(\epsilon M_1) + f\left(\log\,\left(\frac{M_{\rm vir}}{M_1}\right)\right) - f(0) - \log\, M_{\rm vir} \tag{10}$$

where ϵ, M_1, and the function f are heavily involved parameters.The exact details of this parameterization can be found in Behroozi et al. (2013). We take this fit at only z = 6 and apply for all redshifts to maintain continuity for all mass ranges. Figure 2 shows the combined fits of f_* at various redshifts. In order to remove discontinuities in combining the two fits, we extrapolate Eq. 9 until $f_* = 0.022$, or equal to the maximum of Eq. 10 at z = 6. Then we assume a constant f_* in the range between the two fits to connect them continuously. This imposed ceiling is largely consistent with the results from high-redshift numerical simulations which show a maximum stellar fraction (Hopkins et al. 2014; Kimm & Cen 2014; Schaye et al. 2014; Pawlik et al. 2016).

One component in the ζ for galaxies that is not in the ζ for mini-halos is the halo occupation fraction, $f_{\rm occ}$. This parameter takes into account for the fact that not every halo has a stellar population that provides ionising photons. Thus, it dampens the contribution from young low-mass halos which have bursty star formation periods. This relation is given by

$$f_{\rm occ}(M_{\rm h}) = \left[1 + \left(2^{\alpha/3} - 1\right) \left(\frac{M_{\rm h}}{M_{\rm c}} \right)^{-\alpha} \right]^{-3/\alpha} \tag{11}$$

taken from O'Shea et al. (2015) based on the form from Okamoto et al. (2008) where $\alpha = 1.5$ and $M_{\rm c} = 6.0$ x $10^7\,{\rm M}_\odot$. This function exponentially drops off below 1 for masses below the characteristic mass, $M_{\rm c}$. Above this mass, the fraction quickly approaches unity implying every halo contains ionising sources. Finally, we take $N_{2,\gamma/{\rm b}}$ to be a constant 4000 photons per baryon (Schaerer 2003).

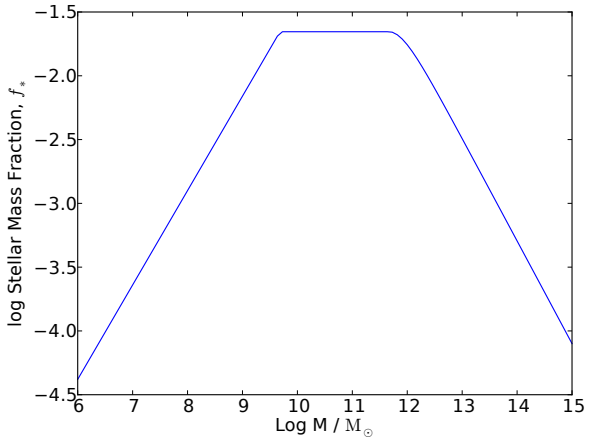

Figure 2. Stellar mass fraction as a function of host halo mass. The lower mass end power law is taken from O'Shea et al. (2015) while the high mass end is taken from Behroozi et al. (2013) at z = 6. We approximate the stellar mass fraction in the central mass ranges to be equivalent to the peaks of both ends to maintain continuity.

2.2.3 Putting it Together

Figure 3 shows ζ as a function of halo mass for a number of redshifts. The biggest contribution in the range $9 \leq$ log $M_{\rm vir}/\,{\rm M}_\odot < 12$ is due to the peaking of f_*. These galaxies have large f_* while still having $f_{\rm esc} > 0.1$ and thus provide the largest fraction of ionising photons. For log $M_{\rm vir}/\,{\rm M}_\odot > 12$, star formation becomes inefficient represented by a steep decline in ζ. At the lower mass end below log $M_{\rm vir}/\,{\rm M}_\odot < 8$, the star forming halo occupation fraction greatly depresses ζ. Because we assume redshift-independent star formation parameters for ζ above the filtering mass, we see the values of ζ overlapping.

Given these distributions, we take a weighted average to get a single ζ value for a given redshift. First, we take the halo mass function (HMF) at a given redshift. We use the following form

$$\frac{dn}{dM} = f(\sigma) \frac{\bar{\rho}_m}{M} \frac{d\,\ln\,\sigma^{-1}}{dM} \tag{12}$$

taken from Tinker et al. (2008) calculated using the python software package Rabacus (Altay & Wise 2015). We then normalize the HMF at $M_{\rm min}(z)$ to be 1. Now we can define $n_{\rm frac}$ to be the fraction of halos at a mass range between M and $M + dm$ by taking the difference of the normalized HMF at those values.

We can then take the integrated average of ζ weighted by halo number density fraction and halo mass as

$$\zeta(z) = \frac{1}{1 + n_{\rm rec}} \frac{\int_{M_{\rm min}}^{M_{\rm max}} \zeta(M_{\rm h})\; n_{\rm frac}\; M_{\rm h}\; dm}{\int_{M_{\rm min}}^{M_{\rm max}} n_{\rm frac}\; M_{\rm h}\; dm} \tag{13}$$

where $n_{\rm frac}$ is the fraction of halos within a mass range between $M_{\rm h}$ and $M_{\rm h} + dm$. We find take $M_{\rm max} = 10^{15}\,{\rm M}_\odot$ to consider the full range of halo masses. This integral is similar to that introduced in Furlanetto et al. (2005), where they took

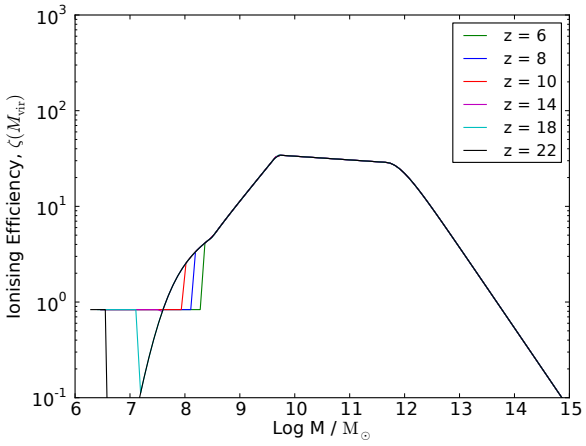

Figure 3. Ionising efficiency, ζ, as a function of host halo mass at various redshifts. For masses $M_{min} \leq M_{vir} < M_{filter}$, we assume Pop III stars are the dominant ioinisation sources and assume a constant ζ. Both M_{min} and M_{filter} evolve with redshift and the latter acts a moving threshold between mini-halos and galaxies. For galaxies, we take the distribution of ionising efficiencies as a function of the halo mass to be independent of redshift. The values of ζ all overlap above M_{filter} as we assume a redshift-independent f_* for galaxies.

ζ to have a power-law dependence on the host halo mass instead.

Furthermore, we introduce a mean recombination number per baryon as

$$n_{rec} = C(z)\ t_{H,0}\ \alpha_B\ \bar{n}_{H,0}\ (1+z)^{3/2} \tag{14}$$

where $t_{H,0}$ is the Hubble time at the present day, $\bar{n}_{H,0}$ is the mean hydrogen number density at the present day, and α_B is the case B recombination coefficient at 10^4 K which is taken as 2.6 x 10^{-13}cm^3 s^{-1}. As our treatment of the recombination number is a global value that only depends on redshift, and not on the halo mass, we can safely evaluate it outside the integral. We also include the clumping factor given by

$$C(z) = \begin{cases} 1 + \exp(-0.28z + 3.50) & z \geq 10 \\ 3.2 & z < 10 \end{cases} \tag{15}$$

taken from Pawlik et al. (2008) to account for the boosted recombination rates in a clumpy IGM. An increased recombination rate requires an increased number of photons to keep the IGM reionised which has the effect of dampening ζ overall. This is in contrast to the method of Sobacchi & Mesinger (2014) where the recombination rate was calculated in each cell to produce the time-integrated number of recombinations per baryon to adjust ζ. We find, however, that both treatments result in a similar effect.

Finally, we can then calculate a ζ for any given redshift. Figure 4 shows the calculated ζ as a function of redshift. The line shows a polynomial fit to ζ with the functional form given by

$$\zeta(z) = A + Bz^2 + Cz^2 + Dz^3 + Ez^4 \tag{16}$$

Table 1. Coefficients for fits of ζ

Model	A	B	C	D	E
Mean	30.27	-6.293	0.506	-1.801 x 10^{-2}	-2.366 x 10^{-4}
Lo	14.74	-3.088	0.248	-8.902 x 10^{-3}	-1.189 x 10^{-4}
Hi	51.71	-1.061	0.852	-2.995 x 10^{-2}	-3.820 x 10^{-4}

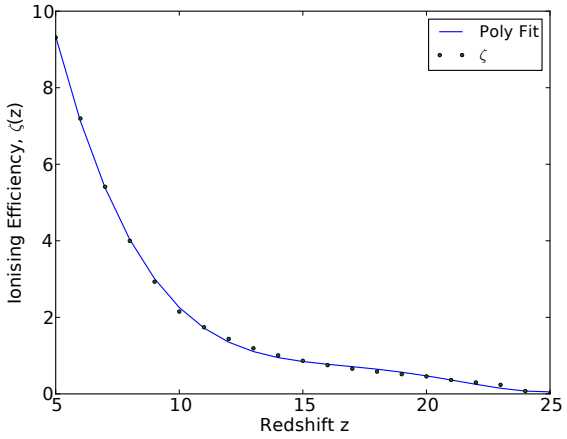

Figure 4. Integrated ionising efficiency ζ as a function of redshift. The dots show the calculated ζ values at each redshift while the line shows a 4th-order polynomial fit. See Eq. 16 for the fit parameters. At high-z, the contribution from mini-halos dominates and suppresses ζ. At low-z, massive galaxies begin to dominate and greatly increases the ionising efficiency.

where the coefficients are shown in Table 1. At high redshifts, ζ remains mostly constant. This is because at these redshifts, the vast majority of ionising sources are mini-halos whose ionising efficiencies we have taken to be a constant value significantly lower than that of galaxies. These smaller objects form smaller H II regions and thus cover only a small volume fraction of the total universe. In contrast, the general trend shows an exponential increase in the ionising efficiency at lower redshifts. Recall that the ionising efficiencies peak in the range $9.5 < \log M_{vir}/M_\odot < 12$. At these lower redshifts, the number of halos available to produce ionising photons at these mass ranges continually increases as halos merge to form larger structures which results in the boosted ζ. These galaxies with large f_* provide the bulk of ionising photon budget necessary for reionisation. We stress that Eq. 16 is only valid for the range $5 < z < 25$ as all the parameters have been calibrated from high-redshift simulations.

2.2.4 Quantifying the Uncertainties

In order to consider the full range of values given the large uncertainties in certain parameters, we calculated the upper and lower limits to ζ as a function of redshift. Table 2 shows the list of parameters that we have chosen to vary along with the range. The greatest variances are in f_{esc} reported by Wise et al. (2014) and Kimm & Cen (2014). For f_{t*}, we assume the same lifetime for Pop III stars and only vary the recovery times as reported by Muratov et al. (2012) and Jeon et al.

Table 2. Varied parameters and their values

Parameter	Mean Value	Lo Value	Hi Value
Pop III $f_{\rm esc}$	0.6	0.05	0.9
f_{t*}	$\frac{5\ \rm Myr}{30\ \rm Myr}$	$\frac{5\ \rm Myr}{100\ \rm Myr}$	$\frac{5\ \rm Myr}{10\ \rm Myr}$
Galaxy $f_{\rm esc}$	$f_{\rm esc}(M_{\rm h})$	$f_{\rm esc}(M_{\rm h})$ x 0.7	$f_{\rm esc}(M_{\rm h})$ x 1.3
Galaxy f_*	$f_*(M_{\rm h}, z)$	$f_*(M_{\rm h}, z)$ x 0.7	$f_*(M_{\rm h}, z)$ x 1.3

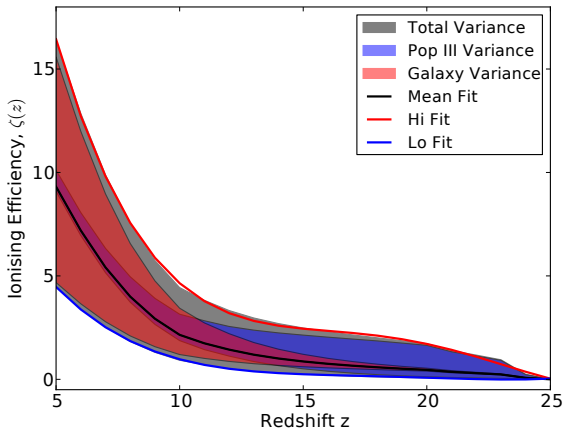

Figure 5. Integrated ionising efficiency ζ as a function of redshift including the spread using both low and high limit values for the various parameters in Eq. 3. The blue and red shaded regions show the spread of ζ due to Pop III and galaxies respectively, while the grey shows the total spread due to the combined variance. The lines also show the polynomial fit to each of the Lo (blue), Hi (red), and Mean (black) values of ζ.

(2014). For the galactic f_*, we take the average variances found in Behroozi et al. (2013). All other parameters not listed in the table remain as their original definitions.

These values are used to produce the ionisation fields for the upper, lower, and standard values of ζ. They provide a first order approximation to the possible distribution of ζ values. For both the lower and upper limits, we take a polynomial fit of the same form as Eq. 16 to calculate ζ. The coefficients for the resulting fits are found in Table 1.

Figure 5 shows the corresponding variances in the ζ function. The blue shaded region shows the resulting variance due to Pop III parameters while the red region shows it for galaxies. The effective combined range of values are represented by the grey area. At high redshifts (i.e. z > 15), the spread is entirely blue indicating only the mini-halos contribute significantly to the photon budget. As structure formation continues, the galactic contribution dominates after z < 10. This is expected as the Pop III star formation rate plateaus as their own formation results in the metal-enrichment of their surroundings suppressing further Pop III formation (Wise et al. 2012b; Xu et al. 2016b) . Instead, these mini-halos merge together to assemble galaxies with greater star formation rates and larger collapsed structures. Once reionisation is fully underway, the galactic contribution increases exponentially which also increases the spread of uncertainties at lower redshifts (Sharma et al. 2016).

3 RESULTS

We run a total of four simulations from the same cosmological initial conditions at z = 300 each with varying ζ . The high resolution density grid is sampled by 2048^3 cells which is smoothed over a 1024^3 grid to produce the ionisation field. We produce 50 snapshots equally spaced in time starting from z = 25 down to z = 6 to produce the entire ionisation history. The fiducial case takes the three parameter model from Greig & Mesinger (2016) consisting of $T_{\rm vir}^{\rm min}$, the minimum virial temperature hosting ionising sources, ζ, the ionisation efficiency, and $R_{\rm mfp}$, the maximum horizon for ionising photons which defines the maximum filtering scale. From their results, we take the best fit values for each of the parameters which are $T_{\rm vir}^{\rm min} = 10^5$ K, $\zeta = 50$, and $R_{\rm mfp} = 20$ Mpc.

In comparison with the fiducial case, we run a total of three simulations with varying values of ζ as a function of redshift. In each of the runs, rather than taking the minimum virial temperature as a proxy for the minimum mass of ionising halos, we use the minimum mass calculated by Eq. 4. The three runs are then the Mean, Hi, and Lo cases which represent the base fit to ζ and its upper and lower variance values with their fits given in Table 1. We keep the same maximum horizon as $R_{\rm mfp} = 20$ Mpc as Sobacchi & Mesinger (2014) and Greig & Mesinger (2016) have shown that the resulting ionisation fields are largely insensitive to the choice.

3.1 Reionisation Histories

Figure 6 shows the ionisation histories calculated from each of the four runs. We define the start of reionisation, $z_{\rm start}$, to be when the ionised fraction, $x(z)$, is at 10%. Similarly, the end, $z_{\rm end}$, is when $x(z) = 99\%$. The blue line shows the fiducial case which does not quite end up fully ionised at the end at z = 6.0, while $z_{\rm start} = 9.8$. The green line shows the Mean case which also has $z_{\rm start} = 9.8$ and $z_{\rm end} = 6.0$. The fiducial model has a much steeper rise at $z_{\rm start}$ while the Mean case shows a gradual rise in the ionised fraction. In the former, as only halos with $T_{\rm vir} > 10^5$ K are considered, there is a more abrupt increase in the ionised fraction as these halos do not exist in large numbers until lower redshifts. In the latter, as mini-halos begin forming early on at high redshifts, there is a gradual increase in the ionised fraction as Pop III stars continually add on to the photon budget. Moreover, since the value of ζ is relatively sensitive to Pop III parameters at $z \sim 10$, mini-halos must play a role in determining the exact starting point of reionisation. Once reionisation is underway, the Mean case shows a steeper increase in the ionised fraction resulting in a slightly earlier end to the EoR. This is mostly due to the steep incline in ζ at these low redshifts corresponding to the presence of bigger halos with large f_* emitting a significant amount of ionising photons.

The shaded region in green shows the spread in histories where the edges represent the Hi and Lo value cases. The Hi value case has $z_{\rm start} = 11$ and $z_{\rm end} = 6.9$ while the Lo value case has $z_{\rm start} = 8.8$ and only reaches x = 0.45 at z = 6. Given the constraint that the universe is fully ionised by z = 6, much of the lower spread in histories is effectively ruled out. This broadly constrains our parameters, in particular $f_{\rm esc}$ and f_* for galactic populations. However, even considering

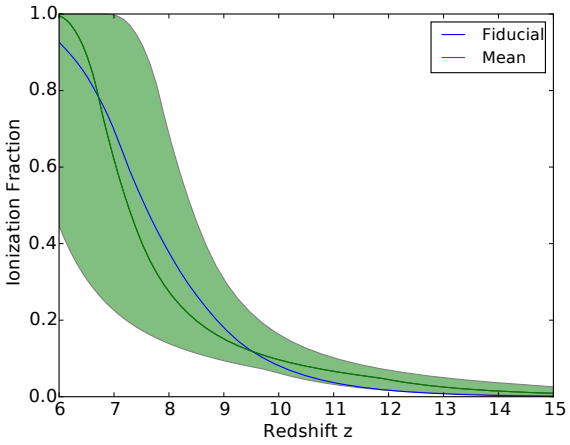

Figure 6. Ionisation histories of all four runs. The blue line represents the fiducial run using the three parameter model from Greig & Mesinger (2016). The green line shows the Mean value run using our new parameterization. The shaded region shows the spread in ionisation histories using our Lo and Hi value parameterizations.

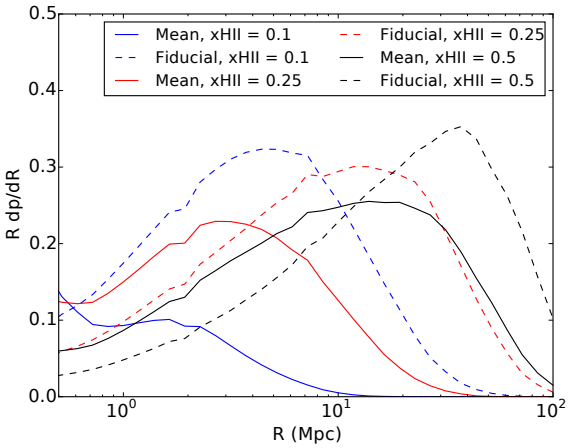

Figure 7. Bubble size distributions at $x \approx 0.1$ (blue), $x \approx 0.25$ (red), $x \approx 0.5$ (black) . The Mean case is represented with solid lines and the Fiducial with dashed lines. The dip and peak at R $\sim$ 2 Mpc and $\sim$ 8 Mpc are artifacts from the numerical bubble size distribution calculation.

just the Hi case, there is a broad range of $z_{\rm start}$ as the large mini-halo population quickly drives up the ionised fraction to the threshold fairly early on.

We also calculate the optical depth due to Thomson scattering for each of the runs by

$$\tau_e = \int_0^\infty dz \frac{c(1+z)^2}{H(z)} x(z)\sigma_{\rm T}\bar{n_{\rm H}}(1+\eta Y/4X) \quad (17)$$

where H(z) is the Hubble parameter, $x(z)$ is the ionised fraction of hydrogen, $\sigma_{\rm T}$ is the Thomson cross-section, and X and $Y = 1-X$ are the hydrogen and helium number fractions respectively. We also assume that helium is singly ionised (η = 1) at z > 3 and doubly ionised at later times ($\eta = 2$).

The fiducial case produces $\tau_e = 0.0567$ while the Mean case has $\tau_e = 0.0569^{+0.0121}_{-0.0125}$, where the Hi and Lo case τ_e are represented as uncertainties. Taking the estimated value from the *Planck* 2016 intermediate results of $\tau_e = 0.0596 \pm 0.0089$ (Planck Collaboration et al. 2016b), we see that our value is still well within the margin of error albeit lower.

3.2 Bubble Size Distributions

In order to further characterize the differences between our models, we generate ionised bubble size distributions. These distributions tell us about the morphology of reionisation as the H II regions grow and expand. We use the same methodology found in Mesinger & Furlanetto (2007) to maintain consistency in generating the distributions. First, we smooth out the ionisation field and remove the partial ionisation values by setting a threshold. We choose this threshold to be 0.5. We then choose an ionised cell and a direction vector at random and measure the distance to the nearest neutral cell. We repeat the process 10^7 times to get a distribution. This method has been shown to be a good approximation to getting the true distributions (Lin et al. 2015).

Figure 7 shows the generated bubble size distributions for the Mean and Fiducial cases at different ionisation fractions. At any given ionisation fraction, the peak in the distribution function, or characteristic size, of the Mean model is at a lower value compared to the Fiducial case. This can be understood as due to the presence of mini-halos which make up a larger fraction of ionised cells in our model driving the peak down. These mini-halos have small ionising photon luminosities, which would correspond to smaller H II regions. We also see a broadening of the peaks as x increases, which can be attributed to the heightened number of mergers of the bubbles. There are a larger number of small bubbles that merge with the larger bubbles that artificially increase the size. At high x, the characteristic size quickly approaches the size of the box in both cases as expected.

Recently Paranjape & Choudhury (2014) showed that a correction to remove the correlation in the random walk introduced by the smoothing filter can result in a significant increase in the characteristic sizes. We expect a similar impact should the correction be included.

4 DISCUSSION AND SUMMARY

The greatest strength in our parameterization is that the assumed values are those constrained by the latest numerical simulations including full range of physical process including radiative and supernova feedback effects. This enables us to consider the full range of mass scales rather than assuming a single ionising efficiency for all halos. However, one large downside to this particular semi-numerical treatise is that the method is still fundamentally a single parameter model that only depends on the collapse mass fraction. There is no consideration of the environment that the sources live in, whether it is in a ionised region or not, and we take a relatively crude average over all halos in different environments to get a single efficiency coefficient. This may result in an improper weighting of ζ. This is a problem that is well treated in contrast in full radiation hydrodynamics simula-

tions, which is now starting to be computationally feasible at large scales (Ocvirk et al. 2015).

A number of instruments will be coming online within the next several years to help put tighter constraints on models of reionisation. 21 cm interferometry performed by the Square Kilometer Array (SKA)[1] and the Hydrogen Epoch of Reionization Array (HERA)[2] will produce accurate mapping of the morphology of the reionisation process. Moreover, the James Webb Space Telescope should extend the current limits to the luminosity function of galaxies constraining parameters such as the stellar mass fraction. With these observations, we expect that our models can be utilized to study the onset of reionisation.

In this work, we extended the semi-numeric simulation code 21cmFAST to include a redshift-dependent minimum mass threshold for ionising source containing halos, $M_{\rm min}$, as well as a mass- and redshift-dependent ionising efficiency, ζ. Our model produces reionisation histories that have subtle differences in comparison with the default model implemented in 21cmFAST while still being broadly consistent with the constraints from *Planck*. Moreover, we find significant differences in the bubble size distribution due to the presence of mini-halos which drive the characteristic scales down. We find that our model broadly constrains the minimum ionising efficiency contribution from galaxies while mini-halos only contribute near the beginning of reionisation, having no significant impact after z = 10.

ACKNOWLEDGEMENTS

We thank Andrei Mesinger for making 21cmFast publicly available. This research was supported by National Science Foundation (NSF) grants AST-1333360 and AST-1614333 and Hubble theory grants HST-AR-13895 and HST-AR-14326.

REFERENCES

Abel T., Bryan G. L., Norman M. L., 2002, Science, 295, 93
Abel T., Wise J. H., Bryan G. L., 2007, ApJ, 659, L87
Ahn K., Iliev I. T., Shapiro P. R., Mellema G., Koda J., Mao Y., 2012, ApJ, 756, L16
Altay G., Wise J., 2015, Astron. Comput., 10, 73
Alvarez M. A., Bromm V., Shapiro P. R., 2006, ApJ, 639, 621
Alvarez M. A., Finlator K., Trenti M., 2012, Astrophys. J. Lett., 759
Becker G. D., Bolton J. S., Madau P., Pettini M., Ryan-Weber E. V., Venemans B. P., 2015, MNRAS, 447, 3402
Behroozi P. S., Wechsler R. H., Wu H.-Y., Busha M. T., Klypin A. A., Primack J. R., 2013, ApJ, 763, 18
Fan X., et al., 2006, ApJ, 132, 117
Furlanetto S. R., Zaldarriaga M., Hernquist L., 2004, ApJ, 613, 1
Furlanetto S. R., McQuinn M., Hernquist L., 2005, MNRAS, 365, 115
Gnedin N. Y., 2000, ApJ, 542, 535
Greif T. H., Johnson J. L., Bromm V., Klessen R. S., 2007, ApJ, 670, 1
Greif T. H., Springel V., White S. D. M., Glover S. C. O., Clark P. C., Smith R. J., Klessen R. S., Bromm V., 2011, ApJ, 737, 75
Greig B., Mesinger A., 2016, The Global History of Reionisation (arXiv:1605.05374)
Grissom R. L., Ballantyne D. R., Wise J. H., 2013, A&A, 561
Gunn J. E., Peterson B. A., 1965, ApJ, 142, 1633
Heger A., Woosley S. E., 2002, ApJ, 567, 532
Heger A., Woosley S. E., 2010, ApJ, 724, 341
Hirano S., Hosokawa T., Yoshida N., Omukai K., Yorke H. W., 2015, MNRAS, 448, 568
Hopkins P. F., Keres D., Onorbe J., Faucher-Giguere C.-A., Quataert E., Murray N., Bullock J. S., 2014, MNRAS, 445, 581
Iliev I. T., Mellema G., Shapiro P. R., McDonald P., Pen U.-L., 2007, Edge Universe Latest Results from Deep. Astron. Surv. ASP Conf. Ser., 380
Iliev I. T., Mellema G., Ahn K., Shapiro P. R., Mao Y., Pen U.-L., 2014, MNRAS, 439, 725
Jeon M., Pawlik A. H., Bromm V., Milosavljevic M., 2014, MNRAS, 444, 3288
Kimm T., Cen R., 2014, ApJ, 788, 121
Kitayama T., Yoshida N., Susa H., Umemura M., 2004, ApJ, 613, 631
Koh D., Wise J. H., 2016, MNRAS, 462, 81
Kuhlen M., Faucher-Giguere C. A., 2012, MNRAS, 423, 862
Lin Y., Oh S. P., Furlanetto S. R., Sutter P. M., 2015, MNRAS, 461, 3361
Machacek M. E., Bryan G. L., Abel T., 2001, ApJ, 548, 509
Madau P., Haardt F., 2015, Astrophys. J. Lett., 813, L8
Madau P., Haardt F., Rees M. J., 1999, ApJ, 514, 648
Mesinger A., 2010, MNRAS, 407, 1328
Mesinger A., Furlanetto S., 2007, ApJ, 669, 663
Mesinger A., Furlanetto S., Cen R., 2011, MNRAS, 411, 955
Muratov A. L., Gnedin O. Y., Gnedin N. Y., Zemp M., 2012, ApJ, 772, 13
O'Shea B. W., Wise J. H., Xu H., Norman M. L., 2015, ApJ, 807, L12
Ocvirk P., et al., 2015, MNRAS
Okamoto T., Gao L., Theuns T., 2008, MNRAS, 390, 920
Paardekooper J.-P., Khochfar S., Vecchia C. D., 2015, MNRAS, 451, 2544
Paranjape A., Choudhury T. R., 2014, MNRAS, 442, 1470
Pawlik A. H., Schaye J., van Scherpenzeel E., 2008, MNRAS, 394, 1812
Pawlik A. H., Rahmati A., Schaye J., Jeon M., Vecchia C. D., 2016, eprint arXiv:1603.00034
Planck Collaboration et al., 2016a, Planck 2016 intermediate results. XLVII. Planck constraints on reionization history (arXiv:1605.03507), http://arxiv.org/abs/1605.03507
Planck Collaboration et al., 2016b, Planck intermediate results. XLVI. Reduction of large-scale systematic effects in HFI polarization maps and estimation of the reionization optical depth (arXiv:1605.02985), http://arxiv.org/abs/1605.02985
Robertson B. E., Ellis R. S., Dunlop J. S., McLure R. J., Stark D. P., 2010, Nature, 468, 49
Schaerer D., 2002, A&A, 382, 28
Schaerer D., 2003, A&A, 397, 527
Schaye J., et al., 2014, MNRAS, 446, 521
Sharma M., Theuns T., Frenk C. S., Bower R. G., Crain R. A., Schaller M., Schaye J., 2016, MNRAS, 458, L94
Sobacchi E., Mesinger A., 2014, MNRAS, 440, 1662
Susa H., Hasegawa K., Tominaga N., 2014, ApJ, 792, 32
Tinker J. L., Kravtsov A. V., Klypin A., Abazajian K., Warren M. S., Yepes G., Gottlober S., Holz D. E., 2008, ApJ, 688, 709
Trac H., Gnedin N. Y., 2011, Adv. Sci. Lett., 4, 228

[1] http://www.skatelescope.org/
[2] http://reionization.org

Tumlinson J., Shull J. M., 2000, ApJ, 528, L65
Turk M. J., Abel T., O'Shea B., 2009, Science, 325, 601
Whalen D., Abel T., Norman M. L., 2004, ApJ, 610, 14
Willott C. J., et al., 2010, ApJ, 139, 906
Wise J. H., Cen R., 2009, ApJ, 693, 984
Wise J. H., Abel T., Turk M. J., Norman M. L., Smith B. D., 2012a, MNRAS, 427, 311
Wise J. H., Turk M. J., Norman M. L., Abel T., 2012b, ApJ, 745, 50
Wise J. H., Demchenko V. G., Halicek M. T., Norman M. L., Turk M. J., Abel T., Smith B. D., 2014, MNRAS, 442, 2560
Woosley S. E., Weaver T. A., 1995, ApJS, 101, 181
Xu H., Wise J. H., Norman M. L., Ahn K., O'Shea B. W., 2016a, Galaxy Properties and UV Escape Fractions During Epoch of Reionization: Results from the Renaissance Simulations (`arXiv:1604.07842`), `http://arxiv.org/abs/1604.07842`
Xu H., Norman M. L., O'Shea B. W., Wise J. H., 2016b, ApJ, 823
Zahn O., Lidz A., McQuinn M., Dutta S., Hernquist L., Zaldarriaga M., Furlanetto S. R., 2007, ApJ, 654, 12
Zahn O., Mesinger A., McQuinn M., Trac H., Cen R., Hernquist L. E., 2011, MNRAS, 414, 727

This paper has been typeset from a TEX/LATEX file prepared by the author.